

The effect of the LISA response function on observations of monochromatic sources

Alberto Vecchio and Elizabeth D. L. Wickham

School of Physics and Astronomy, University of Birmingham, Edgbaston, Birmingham B15 2TT, UK

(Dated: October 23, 2019)

The Laser Interferometer Space Antenna (LISA) is expected to provide the largest observational sample of binary systems of faint sub-solar mass compact objects, in particular white-dwarfs, whose radiation is monochromatic over most of the LISA observational window. Current astrophysical estimates suggest that the instrument will be able to resolve $\sim 10^4$ such systems, with a large fraction of them at frequencies $\gtrsim 3$ mHz, where the wavelength of gravitational waves becomes comparable to or shorter than the LISA arm-length. This affects the structure of the so-called LISA transfer function which cannot be treated as constant in this frequency range: it introduces characteristic phase and amplitude modulations that depend on the source location in the sky and the emission frequency. Here we investigate the effect of the LISA transfer function on detection and parameter estimation for monochromatic sources. For signal detection we show that filters constructed by approximating the transfer function as a constant (long wavelength approximation) introduce a negligible loss of signal-to-noise ratio – the fitting factor always exceeds 0.97 – for $f \leq 10$ mHz, therefore in a frequency range where one would actually expect the approximation to fail. For parameter estimation, we conclude that in the range 3 mHz $\lesssim f \lesssim 30$ mHz the errors associated with parameter measurements differ from $\simeq 5\%$ up to a factor ~ 10 (depending on the actual source parameters and emission frequency) with respect to those computed using the long wavelength approximation.

I. INTRODUCTION

The Laser Interferometer Space Antenna (LISA) is a space borne laser interferometer of arm-length 5 million km for the observation of gravitational waves (GWs) in the frequency window 10^{-4} Hz - 0.1 Hz [1]. Amongst the great variety of sources that the instrument will be monitoring [2], binary systems of faint sub-solar mass compact objects, in particular white-dwarfs, will be considerably abundant [3, 4, 5, 6]. In fact LISA is expected to provide the largest observational sample of these faint stars; current estimates suggest that $\sim 10^4$ systems will be resolvable [6], including about a dozen of already known galactic binary systems (the so-called "verification sources") easily detectable during the first few weeks of operation. Considerable attention has been recently devoted to (sub-) solar mass binary systems, as they will allow us to investigate the evolutionary history of degenerate stars, their formation rate, distribution in the galaxy and mass transfer [2, 7, 8, 9]. Key issues in preparation of LISA are the design of appropriate data analysis schemes to extract effectively and efficiently signals from noise and the investigation of the astronomical information that can be gathered from the LISA data set, possibly followed up by observations with optical telescopes [10, 11].

Sub-solar mass binary systems are expected to produce a moderate-to-large signal-to-noise ratio in the LISA data set and their radiation is monochromatic over most of the instrument sensitivity window, *i.e.* the intrinsic frequency drift during the observation time $T \approx 1$ yr is smaller than the frequency resolution bin of width $\Delta f = 1/T$ (this of course ignores the spreading of power in adjacent frequency bins induced by the LISA orbital motion around the Sun and the change of orientation of the detector with respect a putative source). In the context of data analysis, both signal detection and parameter estimation, the response of LISA to gravitational waves plays a vital role because it introduces features, such as amplitude and phase modulations, that need to be properly accounted for during signal processing. For LISA, which observes gravitational radiation from binary systems over a frequency band where the signal wavelength λ can be either longer or shorter than the interferometer arm length, $L = 5 \times 10^6$ km, it is well known that the detector response changes dramatically at $f \sim f_* \equiv 1/(2\pi L) \simeq 9.6$ mHz, which corresponds to the inverse of the round-trip light-time along the LISA arms [12]. If $f \ll f_*$ (long-wavelength regime), the instrument transfer function can be effectively regarded as constant while for $f \gtrsim f_*$ the transfer function depends on the source's instantaneous emission frequency and location in the sky, which in turn introduces time and frequency dependent amplitude and phase modulations at the detector output. The LISA transfer function, then, starts to substantially change the structure of the LISA Michelson observable right at the heart of the instrument's sensitivity window $f \approx 3$ mHz [13], and yet the implications for data analysis have been so far largely ignored. In the context of signal detection, no study has been devoted to the identification of the frequency range over which it is indeed safe (with respect to losses of signal-to-noise ratio) to approximate the transfer function as a constant in generating signal templates (which would clearly reduce the complexity of the problem at hand). As far as parameter estimation is concerned, a number of studies have been carried out so far for monochromatic sources aimed at computing lower bounds to the the errors associated with parameter measurements [7, 8, 9, 14]. However, in all of them the LISA transfer function has been treated as a constant. Such a simplifying assumption is likely to affect the evaluation of the actual accuracy with

which source parameters can be measured, and has already been pointed out in the context of observations of massive black hole binary systems [15].

The goal of this paper is to investigate the effect of the LISA transfer function on signal detection and parameter estimation for monochromatic sources. In particular (i) we identify the frequency window over which signal templates can be safely constructed by approximating the transfer function as a constant (i.e. the signal-to-noise ratio is very marginally affected) and (ii) explore the implication of the frequency dependent transfer function on the errors of parameter measurements. For signal detection, the main outcome of our work is that one can safely work in the long-wavelength approximation well into the regime where one would actually expect the approximation to fail: effectively the use of templates computed using the long-wavelength approximation does not introduce any significant loss of signal-to-noise ratio up to $f \approx 10$ mHz. For parameter estimation we conclude that at $f \approx 5$ mHz the errors are already starting to depart, by $\approx 5\% - 10\%$, from those computed using the long wavelength approximation. Such discrepancy becomes more pronounced, on average, as the signal emission frequency increases, and in the frequency range 10 mHz $\leq f \leq 30$ mHz the errors are considerably smaller (up to a factor ~ 10 for the 3-armed LISA) than the ones previously reported in the literature.

The paper is organised as follows: in Section II we review the signal detected at the output of the LISA Michelson interferometer in the so-called long-wavelength approximation (constant transfer function) and rigid adiabatic approximation (frequency dependent transfer function); Sections III and IV contain the key results of the paper: in Section III we estimate the degradation of signal to noise ratio (as a function of frequency) introduced by searching for signals using templates that approximate the transfer function as a constant; in Section IV we show the effects of the LISA transfer function on parameter estimation by computing the inverse of the Fisher information matrix; in both cases we perform extensive Monte Carlo simulations in order to sample a wide parameter space; Section V contains our conclusions and pointers to future work.

II. THE SIGNAL MEASURED AT THE LISA OUTPUT

LISA consists of a constellation of three drag-free spacecraft placed at the vertices of an ideal equilateral triangle with sides $L \simeq 5 \times 10^6$ km to form a three-arm interferometer, with a 60° angle between two adjacent laser beams. The barycentre of the instrument follows an almost circular heliocentric orbit (the eccentricity is < 0.01), 20° behind the Earth; the detector plane is tilted by 60° with respect to the Ecliptic and the instrument counter-rotates around the normal to the detector plane with the same period 1 yr (we refer the reader to [1, 7, 13] and references therein for more details). Due to the finite arm length, the round-trip light-travel time between two vertices of the constellation is finite and this introduces a characteristic frequency defined as:

$$f_* \equiv \frac{1}{2\pi L} \simeq 9.6 \times 10^{-3} \text{ Hz}. \quad (1)$$

The LISA ‘‘Michelson output’’ is synthesised in software using a technique known as Time Delay Interferometry (TDI) by combining the Doppler readouts registered at several points in the LISA constellation [16]. The eccentricity of the orbit, the motion of the spacecraft and the finite arm length of LISA affect, in a non trivial way, the detector output generated by metric perturbations induced by impinging GWs (cf Eq. (11)-(39) of [13]). However, two fairly simple approximations to the *exact* LISA output have been derived: (i) the *long wavelength approximation* and (ii) the *rigid adiabatic approximation*. In both cases the eccentricity of the orbit and time dependency of the arms are ignored. In the long wavelength approximation the actual size of LISA’s arms with respect to λ (the wavelength of the impinging radiation) is also neglected, implying that the instrument transfer function is assumed to be constant. This is a very good representation of the LISA output for $f \ll f_*$. In the rigid adiabatic approximation the frequency and source position dependence of the transfer function are fully included; the LISA Michelson output that is derived under these assumptions is an excellent representation of the exact one up to $f \approx 0.5$ Hz, in the sense that the overlap between the exact and approximated output is always ≥ 0.97 [13]. In the remainder of the paper we will therefore consider the rigid adiabatic approximation as a faithful representation of the signal extracted at the LISA output, as we are considering binary systems whose radiation is at $f < 0.5$ Hz. We refer the reader to [1, 7, 12, 13] and references therein for more details. Here we briefly review, mainly to establish notation, the expressions of the signal recorded at the output of the LISA Michelson interferometer using these two different approximations.

Consider a generic gravitational wave source whose position in the sky, with respect to an observer on LISA, is identified by the unit vector $\hat{\mathbf{N}}$. Gravitational waves travel in the $-\hat{\mathbf{N}}$ direction, and are described by the two independent polarisations h_+ and h_\times [17]. The metric perturbation h_{ab} at the detector can be decomposed as the sum of the two independent polarisation states according to

$$h_{ab}(t) = h^+(t)\epsilon_{ab}^+(t) + h^\times(t)\epsilon_{ab}^\times(t), \quad (a, b = 1, 2, 3), \quad (2)$$

where ϵ_{ab}^+ and ϵ_{ab}^\times are the wave's polarisation tensors. They can be expressed as a function of the source basis tensors, e_{ab}^+ and e_{ab}^\times , and the wave polarisation angle ψ as:

$$\epsilon_{ab}^+ = \cos 2\psi e_{ab}^+ - \sin 2\psi e_{ab}^\times, \quad (3a)$$

$$\epsilon_{ab}^\times = \sin 2\psi e_{ab}^+ + \cos 2\psi e_{ab}^\times. \quad (3b)$$

The source basis tensors are constructed by considering two unit vectors m^a and n^a orthogonal to each other and to the wave propagation direction $-\hat{\mathbf{N}}$, in order to form a left-handed Cartesian tern, according to:

$$e_{ab}^+ = m_a m_b - n_a n_b, \quad (4a)$$

$$e_{ab}^\times = m_a n_b + n_a m_b. \quad (4b)$$

If the signal is described by the two polarisation amplitudes $A_+(t)$ and $A_\times(t)$, respectively, and the gravitational phase $\phi_{GW}(t)$, then Eq. (2) becomes

$$h_{ab}(t) = [A_+(t)\epsilon_{ab}^+(t) - iA_\times(t)\epsilon_{ab}^\times(t)] e^{i\phi_{GW}(t)}, \quad (5)$$

where we have explicitly included the dependence on time.

A. The rigid adiabatic approximation

In the so-called *rigid adiabatic approximation* the strain at the detector induced by the metric perturbation, Eqs. (2) and (5), is [13]

$$h(t) = D^{ab}(t) h_{ab}(t), \quad (6)$$

where $D^{ab}(t)$ is the time dependent detector response tensor. If we consider the detector formed by the arms l_j^a and l_k^a – $\hat{\mathbf{l}}_j$ ($j = 1, 2, 3$) are the unit vectors along each of the LISA arms; in a frame attached to the solar system barycentre they are time dependent functions as a consequence of LISA's motion – the detector response tensor reads

$$D^{ab} = \frac{1}{2} (l_j^a l_j^b T_j - l_k^a l_k^b T_k), \quad (7)$$

where

$$\begin{aligned} T_j = & \frac{1}{2} \operatorname{sinc} \left[2\pi \frac{f}{f_*} (1 + l_j^c N_c) \right] \exp \left\{ -i \left[2\pi \frac{f}{f_*} (3 - l_j^c N_c) \right] \right\} \\ & + \frac{1}{2} \operatorname{sinc} \left[2\pi \frac{f}{2f_*} (1 - l_j^c N_c) \right] \exp \left\{ -i \left[2\pi \frac{f}{f_*} (1 - l_j^c N_c) \right] \right\}. \end{aligned} \quad (8)$$

T_j is the instrument transfer function, whose behaviour as a function of time and frequency is shown in Figures 1 and 2. In general, this is a time dependent function which depends on the source location and the instantaneous frequency of the wave; it carries key information about the interferometer arm length through the characteristic frequency f_* , Eq. (1). It is straightforward to check, cf Figures 1 and 2, that for $f/f_* \ll 1$, T_j tends to unity; as the frequency of GWs increases it develops increasingly stronger oscillations. If we ignore the contribution given by the geometry of the detector, the transfer function introduces a phase shift $\gtrsim 1$ rad for $f \gtrsim 5$ mHz (the LISA peak sensitivity is at $f \simeq 3$ mHz). The overlap of the output (6) with the *exact* expression of the LISA readout is greater than 0.97 up to ≈ 0.5 Hz [13], so that we can safely replace the full expression with the rigid adiabatic approximation in the frequency range of interest for this paper (0.1 mHz - 0.1 Hz).

The expression for the detector response tensor, Eq. (7), can be recast in the form

$$D^{ab}(t) = \sum_{n=1}^4 W_n^{ab}(t) e^{-i\xi_n(t)}, \quad (9)$$

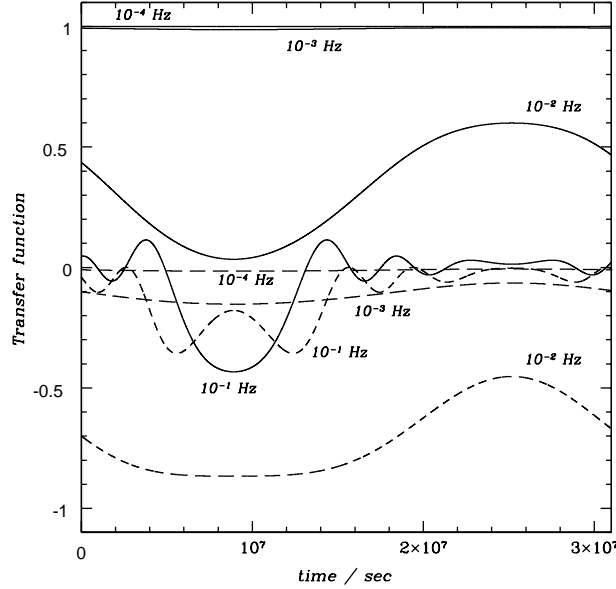


FIG. 1: The time evolution of the LISA transfer function for selected frequencies. The plot shows the transfer function, cf Eq. (8), as a function of time (for one LISA period, corresponding to 1 yr) for one of the arms and a randomly chosen source location. The values of the transfer function for four selected frequencies (see labels) are shown: $f = 10^{-4}$ Hz, 10^{-3} Hz, 10^{-2} Hz and 10^{-1} Hz (solid line: real part; dashed line: imaginary part). Notice that even by $f = 10^{-3}$ Hz the transfer function is no longer constant over the LISA orbital period.

where

$$W_1^{ab} = \frac{1}{4} l_j^a l_j^b \operatorname{sinc} \left[2\pi \frac{f}{f_*} (1 + l_j^c N_c) \right], \quad (10a)$$

$$W_2^{ab} = \frac{1}{4} l_j^a l_j^b \operatorname{sinc} \left[2\pi \frac{f}{2f_*} (1 - l_j^c N_c) \right], \quad (10b)$$

$$W_3^{ab} = -\frac{1}{4} l_k^a l_k^b \operatorname{sinc} \left[2\pi \frac{f}{f_*} (1 + l_k^c N_c) \right], \quad (10c)$$

$$W_4^{ab} = -\frac{1}{4} l_k^a l_k^b \operatorname{sinc} \left[2\pi \frac{f}{2f_*} (1 - l_k^c N_c) \right], \quad (10d)$$

and

$$\xi_1 = 2 \frac{f}{f_*} (3 - l_j^c N_c), \quad (11a)$$

$$\xi_2 = 2 \frac{f}{f_*} (1 - l_j^c N_c), \quad (11b)$$

$$\xi_3 = 2 \frac{f}{f_*} (3 - l_k^c N_c), \quad (11c)$$

$$\xi_4 = 2 \frac{f}{f_*} (1 - l_k^c N_c). \quad (11d)$$

It is also useful to introduce the *generalised antenna beam patterns* $F_n^{(+)}$ and $F_n^{(\times)}$ defined as

$$F_n^{(+)}(t) \equiv W_n^{ab}(t) \epsilon_{ab}^+(t), \quad (12a)$$

$$F_n^{(\times)}(t) \equiv W_n^{ab}(t) \epsilon_{ab}^\times(t). \quad (12b)$$

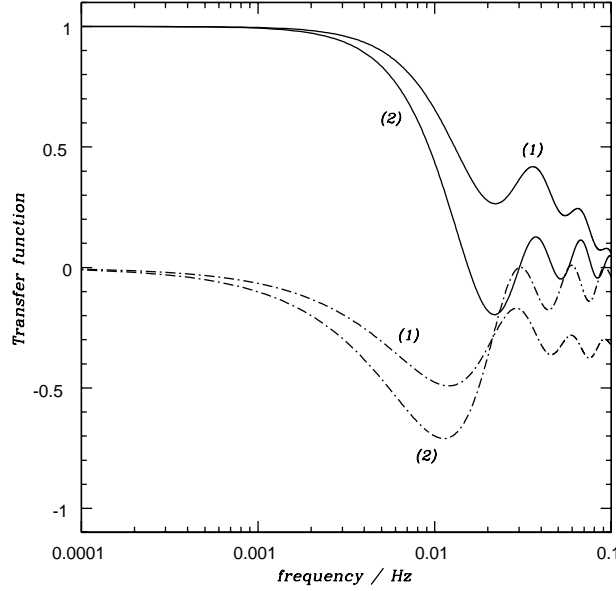


FIG. 2: The frequency dependence of the LISA transfer function. The plot shows the LISA transfer function, cf Eq. (8), as a function of frequency for two (see labels) selected relative positions and orientations of LISA with respect to a source (solid line: real part; dotted-dashed line: imaginary part). Notice that at a few mHz the transfer function is already significantly different from the constant value apparent at $f \ll f_*$.

$F_n^{(+)}$ and $F_n^{(\times)}$ are time dependent because of the change of orientation of LISA during the typical observation time ~ 1 yr. It is straightforward to verify that at low frequencies

$$F_+ = \sum_{n=1}^4 F_n^{(+)} \quad (f \ll f_*) , \quad (13a)$$

$$F_\times = \sum_{n=1}^4 F_n^{(\times)} \quad (f \ll f_*) , \quad (13b)$$

where F_+ and F_\times are the usual antenna beam patterns cf. Eqs. (20a) and (20b).

Using Eqs (2), (9), (10a)-(10d) and (11a)-(11d), the (real) strain at the detector becomes:

$$h(t) = \sum_{n=1}^4 \left(F_n^{(+)}(t) A_+(t) \cos[\phi_{GW}(t) - \xi_n(t) + \varphi_D(t)] + F_n^{(\times)}(t) A_\times(t) \sin[\phi_{GW}(t) - \xi_n(t) + \varphi_D(t)] \right) , \quad (14)$$

where we have included the phase Doppler shift induced in the signal at the LISA output by the motion of the LISA barycentre with respect to a source, see Eq. (A13). Using double angle formulae one can express Eq. (14) as the superposition of 4 harmonics with different (time dependent) polarisation amplitudes and phases

$$h(t) = \sum_{n=1}^4 B_n(t) \cos \chi_n(t) , \quad (15)$$

where

$$B_n(t) = \left[F_n^{(+)}(t) A_+(t) + F_n^{(\times)}(t) A_\times(t) \right]^{1/2} , \quad (16)$$

$$\chi_n(t) = \phi_{GW}(t) - \xi_n(t) + \varphi_D(t) + \varphi_n(t) , \quad (17)$$

and

$$\varphi_n(t) = \arctan \left[-\frac{F_n^{(\times)}(t) A_{\times}(t)}{F_n^{(+)}(t) A_{+}(t)} \right]. \quad (18)$$

Explicit expressions for $B_n(t)$, $\chi_n(t)$ and $\varphi_n(t)$ are given in the Appendix.

B. The long wavelength approximation

In the low frequency region of the LISA sensitivity band, *i.e.* $f/f_* \ll 1$, the transfer function can be approximated as a constant [13], cf Figures 1 and 2; T_j is therefore independent of the signal frequency and source position in the sky. The strain at the detector output, Eq. (6), takes the usual form

$$h_L(t) = h_{+}(t) F_{+}(t) + h_{\times}(t) F_{\times}(t). \quad (19)$$

This expression is known as the *long wavelength approximation* to the detector output. In the previous expression F_{+} and F_{\times} are the antenna beam patterns. If one takes the observable constructed using the two arms identified by $\hat{\mathbf{l}}_j$ and $\hat{\mathbf{l}}_k$, they read

$$F_{+} = \frac{1}{2}(l_j^a l_j^b - l_k^a l_k^b) \epsilon_{ab}^{+}, \quad (20a)$$

$$F_{\times} = \frac{1}{2}(l_1^a l_1^b - l_2^a l_2^b) \epsilon_{ab}^{\times}. \quad (20b)$$

As is the case for $F_n^{(+)}$ and $F_n^{(\times)}$ ($n = 1, \dots, 4$), F_{+} and F_{\times} are time dependent because of LISA's change in orientation with respect to source location during the observation period.

The detector output (19) can be cast in the form

$$h_L(t) = B(t) \cos \chi(t) \quad (21)$$

where

$$B(t) = [F_{(+)}(t) A_{+}(t) + F_{(\times)}(t) A_{\times}(t)]^{1/2}, \quad (22)$$

$$\chi(t) = \phi_{GW}(t) + \varphi(t) + \varphi_D(t), \quad (23)$$

and

$$\varphi(t) = \arctan \left[-\frac{F_{(\times)}(t) A_{\times}(t)}{F_{(+)}(t) A_{+}(t)} \right]. \quad (24)$$

Explicit expressions for $B(t)$, $\chi(t)$ and $\phi(t)$ are given in the Appendix.

III. SIGNAL DETECTION

In this section we investigate the impact of the instrument transfer function on detection. Due to the essentially perfect knowledge of signal waveforms for this class of sources, we assume that the signal processing scheme will be based on a coherent approach, where the data are correlated with a discrete bank of templates to extract the signal from the noise. The goal of this section is to identify the frequency band over which the use of the long-wavelength approximation h_L for signal templates (*i.e.* constant transfer function), cf Eq. (21), does not affect the signal-to-noise ratio (SNR) at which the actual radiation embedded in the detector noise can be detected. At the LISA output, in fact, gravitational waves are modulated by the complex structure of the instrument transfer function and are actually represented by Eq. (15). It has been recently suggested [13] that the long wavelength approximation, $h_L(t)$, is already not a good approximation of the exact detector output at $f \approx 3$ mHz; here we show that for the purpose of detecting monochromatic signals $h_L(t)$ is actually a completely satisfactory approximation at least up to $f \approx 10$ mHz, in the sense that it returns a fitting factor which is always greater than 0.97. We start by briefly reviewing the key concepts

and formulae of signal detection through matched filtering – we refer the reader to [7, 18, 19] and references therein for more details – and then present the results of our analysis.

The signal $s(t)$ registered at the detector output is a superposition of noise $n(t)$ and gravitational waves $h(t; \boldsymbol{\lambda})$,

$$s(t) = h(t; \boldsymbol{\lambda}) + n(t), \quad (25)$$

where $\boldsymbol{\lambda}$ represents the vector of the unknown parameters that characterise the waveform. In the case of monochromatic sources $h(t)$ is fully described by seven independent parameters: signal amplitude A_{GW} , frequency f_0 , arbitrary initial phase at the beginning the observation ϕ_0 , and four angular parameters related to the position of the source in the sky, θ_N and ϕ_N , and the orientation of the orbital plane, θ_L and ϕ_L (we refer the reader to the Appendix where the explicit dependence of $h(t)$ on $\boldsymbol{\lambda}$ is presented). The parameter vector is therefore $\boldsymbol{\lambda} = \{A_{\text{GW}}, \phi_0, f_0, \theta_N, \phi_N, \theta_L, \phi_L\} = \{A_{\text{GW}}, \phi_0, f_0, \boldsymbol{\theta}\}$, where $\boldsymbol{\theta} = \{\theta_N, \phi_N, \theta_L, \phi_L\}$. Our notation reflects the fact that A_{GW} is not a search parameter, as it determines simply the signal-to-noise ratio at which detection is made, f_0 can be easily searched over using the Fast Fourier Transform of the data stream and ϕ_0 is an extrinsic parameter that can be trivially maximised. We assume the noise to be stationary and Gaussian (although we do not expect this condition to be fully met by the actual data), characterised by a noise spectral density $S_n(f)$. In the geometrical approach to signal processing the signal $h(t)$ represents a vector in the signal manifold and the signal parameters $\boldsymbol{\lambda}$ are the coordinates on this manifold. One can introduce the following inner product between two signals v and w [7]:

$$\begin{aligned} (v|w) &= 2 \int_{-\infty}^{+\infty} \frac{\tilde{v}^*(f)\tilde{w}(f)}{S_n(f)} df \\ &= \frac{2}{S_0} \int_{-\infty}^{+\infty} v^*(t)w(t) dt, \end{aligned} \quad (26)$$

where the second equality follows from Parseval's theorem and S_0 is the (essentially constant) noise spectral density at f_0 .

According to the definition (26), the optimal SNR at which h can be detected is

$$\left(\frac{S}{N}\right)_{\text{opt}} = \frac{(h|h)}{\text{rms}[(h|n)]} = (h|h)^{1/2}. \quad (27)$$

If $q(t; \boldsymbol{\Lambda})$ is the family of templates used to search for the class of signals $h(t; \boldsymbol{\lambda})$ – notice that $\boldsymbol{\Lambda}$, the template parameter vector, is not necessarily the same (including its dimensions) as $\boldsymbol{\lambda}$, and q does not necessarily belong to the same manifold as h – the adequacy of the template family q to search for the signal family h is given by the so-called *fitting factor* (FF), defined as [20]

$$\text{FF}(\boldsymbol{\lambda}) = \max_{\boldsymbol{\Lambda}} \left\{ \frac{(h(\boldsymbol{\lambda})|q(\boldsymbol{\Lambda}))}{[(h(\boldsymbol{\lambda})|h(\boldsymbol{\lambda})) (q(\boldsymbol{\Lambda})|q(\boldsymbol{\Lambda}))]^{1/2}} \right\}. \quad (28)$$

By definition $0 \leq \text{FF} \leq 1$, and the effect of an imperfect matching of filters with signals translates into a reduction of the maximum SNR at which a source can be detected according to

$$\left(\frac{S}{N}\right) = \text{FF} \times \left(\frac{S}{N}\right)_{\text{opt}}. \quad (29)$$

It has become standard in the gravitational wave data analysis literature to assume that a family of filters can be considered adequate if $\text{FF} \geq 0.97$, which corresponds to a decrease in detection rate by about 10%; the detection rate, in fact, scales as $(\text{FF})^3$. Analogously, the *match* M is defined as

$$M(\boldsymbol{\theta}, \boldsymbol{\Theta}) = \max_{\Delta f_0, \Delta \phi_0} \left\{ \frac{(h(\boldsymbol{\theta})|q(\boldsymbol{\Theta}))}{[(h(\boldsymbol{\lambda})|h(\boldsymbol{\lambda})) (q(\boldsymbol{\Lambda})|q(\boldsymbol{\Lambda}))]^{1/2}} \right\}, \quad (30)$$

where $\boldsymbol{\theta}$ and $\boldsymbol{\Theta}$ are the parameter vectors of the signal and template, respectively; Δf_0 and $\Delta \phi_0$ represent the mismatch in extrinsic parameters between signal and template. Notice that here we assume the use of the power spectrum as the detection statistic, which implies the need to search explicitly over the four angles $\theta_N, \phi_N, \theta_L$ and ϕ_L . Instead of the power spectrum, one could actually consider the so-called *F*-statistic [21, 22], which requires the maximisation of the detection statistic using a discrete template bank only over the two angles θ_N and ϕ_N . The conclusions of this section are only marginally affected by our choice of detection statistic.

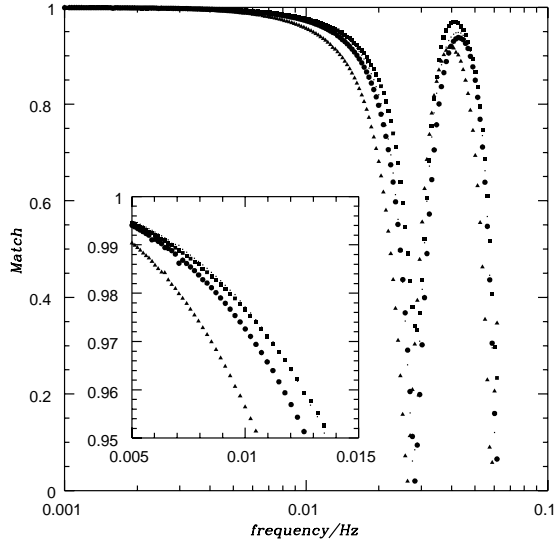


FIG. 3: The frequency dependence of the match. The plot shows the match M , Eq. (30), as a function of frequency, for four randomly selected sky positions and orbital plane orientations (dots: $\theta_N = 2.5$, $\phi_N = 1.4$, $\theta_L = 1.2$, and $\phi_L = 1.4$; squares: $\theta_N = 1.2$, $\phi_N = 4.3$, $\theta_L = 0.36$, and $\phi_L = 4.2$; triangles: $\theta_N = 3.1$, $\phi_N = 0.81$, $\theta_L = 2.7$, and $\phi_L = 0.79$; circles: $\theta_N = 1.8$, $\phi_N = 3.6$, $\theta_L = 1.9$, and $\phi_L = 3.6$). The insert offers a zoom of the region around 10 mHz. The observation time is 1 yr.

We aim to explore the FF for the family of filters constructed using the long wavelength approximation. The FF depends on the point in parameter space at which it is evaluated and its computation requires the maximisation over six parameters, of Eq (28), which in turn translates into a substantial computational burden. In order to investigate extensively the behaviour of templates based on the long wavelength approximation, while keeping the computational time at a manageable level, we have actually evaluated, over an extended portion of the whole parameter space, the match, Eq. (30), which represents a lower limit to the FF, and investigated the FF only for selected points. This strategy has the advantage of reducing substantially the computational burden, while still providing a reasonable approximation to the FF. We therefore set $q = h_L$, cf Eq (21), in Eq. (30) and (28) and the signal is modelled according to Eq. (15). All the results presented here assume that the observation time is $T = 1$ yr.

The match and fitting-factor depend on both frequency and geometric parameters. In general we expect the fitting factor to be essentially unity for $f \ll f_*$, but to drop below 0.97 at some transition frequency whose exact value depends on θ_N , ϕ_N , θ_L and ϕ_L . In order to develop some intuition we begin by computing the match (we set $\Theta = \theta$ in Eq. (30)) for four randomly chosen sky positions and orbital plane orientations as a function of frequency; the results are plotted in Figure 3. It is clear that the match falls below 0.97 only at about 10 mHz and is not a monotonic function of frequency; in fact there is no maximisation over the angular parameters and the impact of the transfer function depends on frequency in a non trivial way. Not surprisingly, the value of the match depends quite significantly on the position and orientation of a source in the sky. To investigate this dependence we select four fiducial frequencies ($f_0 = 3$ mHz, 5 mHz, 10 mHz and 30 mHz) and we compute the match for 1000 randomly chosen sky positions and wave polarisations at each of these frequencies [23]. The results are summarised in Figure 4 and Table I. It is clear that in the frequency range of peak sensitivity of LISA ($f \approx 3$ mHz) the long wavelength approximation is perfectly adequate for signal detection: *all* sources have a match (and *a fortiori* a fitting-factor) larger than 0.99. The frequency $f = 10$ mHz seems to mark the transition to the frequency range over which the exact LISA response is actually needed in order to recover the full SNR. Figure 4 and Table I show that at 10mHz the match for half of the sources is below 0.97, but always greater than ≈ 0.91 . In order to check whether the fitting-factor, the actual figure of merit we are interested in, shows a similar behaviour we have computed FF, Eq. (28), for the three sources that gave the three lowest values of the match, 0.914, 0.927 and 0.928. In all three cases, when the maximisation is carried out over the entire set of parameters, the fitting-factor is raised above 0.97, and yields 0.976, 0.987 and 0.980, respectively. This is a very strong indication that FF is indeed > 0.97 at 10 mHz, and one can

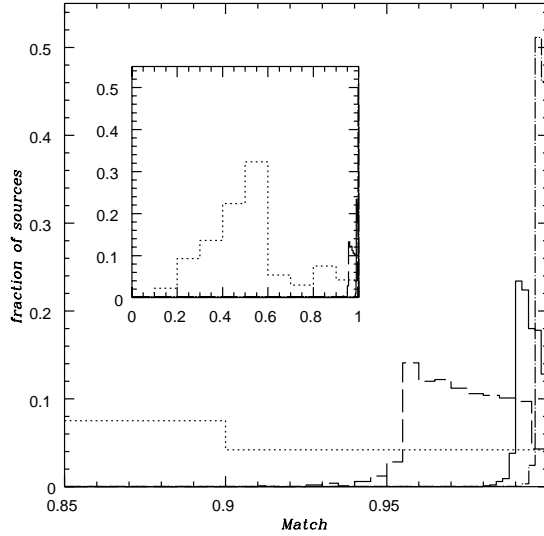


FIG. 4: The distribution of the match. The plot shows the fraction of sources for which a given value of the match is attained: in each Monte Carlo simulation the match is computed for 1000 sources (all emitting at the same frequency) with random sky position and orientation of the orbital plane. Four values of the gravitational wave frequency are presented: $f_0 = 3$ mHz (dotted-dashed line), $f_0 = 5$ mHz (solid line), $f_0 = 10$ mHz (dashed line) and $f_0 = 30$ mHz (dotted line). The observation time is $T = 1$ yr. The inserted panel shows the same results on a different scale for the x -axis in order to cover the whole range of values of the match for $f_0 = 30$ mHz.

consider the long wavelength approximation still adequate at this frequency. However, at 30 mHz the picture changes dramatically and essentially all the sources yield a match which is below 0.97 – the largest match is 0.976 – with the lowest value being as small as 0.074. The mean and median are both ≈ 0.5 . In this case too we have computed the FF for a few sources. Placing the sources in order of ascending match we chose to find FF for the 1st, 2nd, 300th and 700th entries, which gave matches of 0.074, 0.109, 0.432 and 0.558 respectively. As in the case of $f_0 = 10$ mHz the maximisation over all the parameters increases quite substantially the actual value of the FF, in this case to 0.633, 0.614, 0.673 and 0.737 for the 1st, 2nd, 300th and 700th source, respectively. These results indicate that the threshold $FF = 0.97$, which we have set in order to consider the long wavelength approximation as suitable for detection, is not attainable for the large majority of sources. The outcome of our analysis is therefore clear: the long wavelength approximation, $h = h_L$, Eq. (21), can be safely used to construct *detection templates* up to $f_0 = 10$ mHz (for a fitting-factor > 0.97), after which it becomes progressively inaccurate, causing a severe reduction of detection rate; at $f = 30$ mHz the long wavelength approximation is by far inadequate.

IV. PARAMETER ESTIMATION

In this section we discuss the errors associated with the parameter measurements. The estimation of the minimum mean squared errors with which source parameters can be extracted in LISA observations of monochromatic sources has been investigated so far using the long wavelength approximation across the whole LISA observational window [7, 8, 9, 14]. The goal of this section is to explore to what extent the results reported in previous analyses are affected if one actually models the LISA output exactly. Results obtained using the long wavelength approximation are clearly correct at low frequencies ($f \ll f_* \approx 10$ mHz); however they become progressively less representative of what one can actually achieve during the mission in the high frequency portion of the LISA observational window. Here we establish the frequency at which the errors significantly differ depending on the approximation and quantify the discrepancy (as a function of frequency) with respect to previous work. We start by briefly recalling the general concepts and formulae regarding parameter estimation – we refer the reader to [7, 18, 19, 24, 25] and references therein for more

f_0 (mHz)	Match					
	Min.	Max.	Median	Mean	Std. Dev.	Fraction < 0.97
3	0.993	1.000	0.998	0.998	0.001	0
5	0.980	1.000	0.994	0.994	0.003	0
10	0.914	0.999	0.972	0.973	0.014	0.437
30	0.074	0.976	0.506	0.515	0.183	0.998

TABLE I: Statistical summary of the values of the match obtained in each of the Monte Carlo simulations (same as Figure 4) carried out over 1000 random source positions and orientations for a given gravitational wave frequency (shown in the first column of the table). The table shows the minimum (Min.) and maximum (Max.) value of the match, cf Eq. (30), for the different values of the geometrical parameters $\theta_N, \phi_N, \theta_L, \phi_L$ in each Monte Carlo simulation, and well as the (sample) median, mean and standard deviation (Std. Dev.) calculated over the 1000 values in the simulation. The last column shows the fraction of sources for which the match is < 0.97.

details – and then present the results of our analysis.

In the limit of large SNR, which applies to the vast majority of signals considered here, the errors $\Delta\lambda$ associated with the parameters λ that characterise $h(t; \lambda)$ follow a Gaussian probability distribution:

$$p(\Delta\lambda) = \left(\frac{\det(\Gamma)}{2\pi} \right)^{1/2} e^{-\frac{1}{2} \Gamma_{jk} \Delta\lambda^j \Delta\lambda^k}. \quad (31)$$

In Eq.(31) the matrix Γ_{jk} is known as the Fisher information matrix, which reads [7]

$$\Gamma_{jk}^{(\iota)} \equiv \left(\frac{\partial h^{(\iota)}}{\partial \lambda^j} \middle| \frac{\partial h^{(\iota)}}{\partial \lambda^k} \right); \quad (32)$$

the superscript $\iota = I, II$ labels the detector (as pointed out by Cutler in [7], using the three arms of the LISA instrument one can actually construct two observables, $h^{(I)}$ and $h^{(II)}$, respectively, that correspond to two co-located interferometers one rotated by $\pi/4$ with respect to the other with uncorrelated noise.) The *variance-covariance matrix* is simply given by the inverse of the Fisher information matrix:

$$\Sigma^{jk} = \langle \Delta\lambda^j \Delta\lambda^k \rangle = \left[\left(\Gamma^{(\iota)} \right)^{-1} \right]^{jk}. \quad (33)$$

The matrix Σ contains full information about the parameter errors and their correlations; in fact the diagonal elements of Σ represent the expected mean squared errors

$$\langle (\Delta\lambda^j)^2 \rangle = \Sigma^{jj}, \quad (34)$$

and its off-diagonal elements provide information about the correlations among different parameters through the correlation coefficients c^{jk} :

$$c^{jk} = \frac{\Sigma^{jk}}{\sqrt{\Sigma^{jj} \Sigma^{kk}}} \quad (-1 \leq c^{jk} \leq +1). \quad (35)$$

In the limit of high signal-to-noise ratio, Σ^{jj} provides a tight lower bound to the minimum mean-squared error $\langle (\Delta\lambda^j)^2 \rangle$, the so-called Cramer-Rao bound [19, 25]. Notice that the errors (34) and the correlation coefficients (35) depend on the actual value of the signal parameter vector λ . For the case of observations with two or more detectors with uncorrelated noise, the Fisher information matrix is simply: $\Gamma_{jk} = \sum_\iota \Gamma_{jk}^{(\iota)}$. Two parameters we are interested in computing is the error associated with the position of a source in the sky (angular resolution) and the orientation of the orbital angular momentum. Following [7] we define these by

$$\Delta\Omega_{N,L} = 2\pi \left\{ \langle \Delta \cos \theta_{N,L}^2 \rangle \langle \Delta \phi_{N,L}^2 \rangle - \langle \Delta \cos \theta_{N,L} \Delta \phi_{N,L} \rangle^2 \right\}^{1/2}, \quad (36)$$

where N labels position and L labels orientation. The physical meaning of $\Delta\Omega_{N,L}$ is the following: the probability of $\hat{\mathbf{N}}, \hat{\mathbf{L}}$ to lie *outside* an (appropriately shaped) error ellipse enclosing a solid angle $\Delta\Omega$ is simply $e^{-\Delta\Omega/\Delta\Omega_{N,L}}$.

ι	f (mHz)	$(\Delta A/A)_L/(\Delta A/A)$					
		Min.	Max.	Median	Mean	Std. Dev.	Fraction < 1
I	3	0.756	1.642	1.007	1.049	0.124	0.40
	I+II	3	1.010	1.052	1.034	1.033	0.007
I	5	0.752	2.483	1.017	1.127	0.279	0.358
	I+II	5	1.055	1.127	1.096	1.094	0.012
I	10	0.768	6.535	1.065	1.511	1.032	0.303
	I+II	10	1.331	1.541	1.450	1.444	0.036
I	30	0.392	44.164	1.599	4.949	7.696	0.219
	I+II	30	9.539	36.435	15.467	16.769	4.979

TABLE II: Statistical summary of the values of $(\Delta A/A)_L/(\Delta A/A)$ obtained in each of the Monte Carlo simulations carried out over 1000 random source positions and orientations for a given emission frequency (shown in the second column of the table). The table shows the minimum (Min.) and maximum (Max.) value of $(\Delta A/A)_L/(\Delta A/A)$ (see text for more details) for the different values of the geometrical parameters θ_N , ϕ_N , θ_L , ϕ_L in each Monte Carlo simulation, as well as the (sample) median, mean and standard deviation (Std. Dev.) of $(\Delta A/A)_L/(\Delta A/A)$ calculated over the 1000 values in the simulation. The last column shows the fraction of sources for which $(\Delta A/A)_L/(\Delta A/A) < 1$, that is the long wavelength approximation underestimates the errors in the measurement of the signal amplitude. The values are shown both for the case of observations carried out with a single interferometer ($\iota = I$) and with a pair of interferometers ($\iota = I + II$). The observation time is one year. Histograms for the distribution of $(\Delta A/A)_L/(\Delta A/A)$ are presented in Figure 5.

Each element of the Fisher information matrix, cf Eqs (26) and (32) can be written as

$$\Gamma_{jk}^{(\iota)} = \frac{2}{S_0} \int_{-\infty}^{+\infty} \partial_j h^{(\iota)}(t) \partial_k h^{(\iota)}(t) dt, \quad (37)$$

where $\partial_j \equiv \partial/\partial\lambda^j$. Equivalently, the signal-to-noise ratio is given by

$$\left(\frac{S}{N}\right)^{(\iota)} = \frac{2}{S_0} \int_{-\infty}^{+\infty} [h^{(\iota)}(t)]^2 dt. \quad (38)$$

For the problem at hand, for which $f \gg B^{-1}dB/dt$ and $f \gg B_n^{-1}dB_n/dt$, cf Eq. (22) and (16), one can actually simplify the full expression of the Fisher information matrix reducing it to

$$\Gamma_{jk} = \frac{1}{S_0} \int_{-\infty}^{\infty} [\partial_j B(t) \partial_k B(t) + B^2(t) \partial_j \chi(t) \partial_k \chi(t)] dt, \quad (39)$$

in the long-wavelength approximation – $h = h_L$, cf Eq.(21) – and to

$$\begin{aligned} \Gamma_{jk} = & \frac{1}{S_0} \sum_{n,m=1}^4 \int_{-\infty}^{\infty} [\partial_j B_n(t) \partial_k B_m(t) + B_n(t) B_m(t) \partial_j \chi_n(t) \partial_k \chi_m(t)] \cos(\chi_n - \chi_m) \\ & + [A_m(t) \partial_j A_n(t) \partial_k \chi_m - A_n(t) \partial_j A_m(t) \partial_k \chi_n] \sin(\chi_n - \chi_m) dt \end{aligned} \quad (40)$$

in the rigid adiabatic approximation, where h is given by Eq. (15).

LISA parameter estimation for monochromatic signals strongly depends on the actual value of the signal parameters, in particular, emission frequency and location and orientation of a source with respect to the detector. This represents a large parameter space that one needs to explore in order to obtain meaningful results. We perform this exploration by means of Monte-Carlo simulations [23]. For each fiducial source we set f_0 and randomly select the geometrical parameters θ_N , ϕ_N , θ_L , ϕ_L (and the arbitrary initial phase ϕ_0) and compute the inverse of the Fisher information matrix for the cases where h is given by Eq. (21) and Eq. (15). The observation time is set to $T = 1$ yr. The signals are normalised in such a way that they produce the same signal-to-noise ratio in both cases. For each parameter λ^j , we can therefore evaluate the ratio $(\Delta\lambda^j)_L/\Delta\lambda^j$, where the subscript 'L' indicates that the estimated error is computed using the long wavelength approximation for the LISA output; $(\Delta\lambda^j)_L/\Delta\lambda^j$ is independent of SNR, and reflects simply the effect of structure of the transfer function on the estimation of the signal parameters. If the long wavelength approximation is indeed a good approximation for exploring the quality of LISA astronomy, then

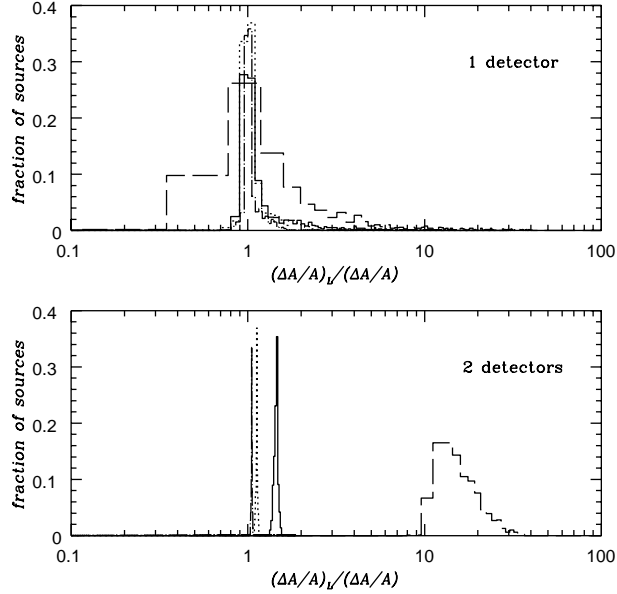


FIG. 5: Distribution of the ratio between the errors associated with measurements of the signal amplitude using the long wavelength approximation and the rigid adiabatic approximation. The histograms show the fraction of sources (out of the 1000, with random position and orientation, used in the Monte Carlo simulations) for which the amplitude can be measured with a fractional error characterised by a given value of the ratio $(\Delta A/A)_L/(\Delta A/A)$, shown on the x -axis (see text for more details). Four histograms are shown, corresponding to different values of the gravitational wave frequency f_0 : 3 mHz (dotted-dashed line), 5 mHz (dotted line), 10 mHz (solid line) and 30 mHz (dashed line). One year of integration is assumed in the computation of the Fisher Information matrix. The top and bottom panels refer to measurements carried out with one and two detectors, respectively. A statistical summary of these results is presented in Table II.

$(\Delta\lambda^j)_L/\Delta\lambda^j = 1$. If $(\Delta\lambda^j)_L/\Delta\lambda^j > 1 (< 1)$ it means that results that have been presented in the literature so far overestimate (underestimate) the errors associated with parameter measurements and one can actually expect better (worse) quality astronomy with LISA.

We have calculated the ratio $(\Delta\lambda^j)_L/\Delta\lambda^j$ for four specific frequencies in the LISA observational window, $f_0 = 3$ mHz, 5 mHz, 10 mHz and 30 mHz (the same values that we adopted in the study of match and fitting factor), for 1000 randomly selected positions and orientations of sources in the sky. We have also considered both the case for one detector and for two detectors at 45° to each other.

We present in detail results for three key parameters: amplitude, angular resolution of $\hat{\mathbf{N}}$ and angular resolution of $\hat{\mathbf{L}}$ in Figures 5, 6 and 7, respectively, and Tables II, III and IV. Each plot is a histogram showing the fraction of sources for which $(\Delta\lambda^j)_L/\Delta\lambda^j$ (where j labels the relevant parameter) falls into each bin (for observations with one and two detectors). The tables provide a statistical summary of the outcome of each Monte Carlo simulation for the three chosen parameters.

The qualitative behaviour of the results is very much consistent with what one would expect: as the frequency of the signal increases the effect of the LISA transfer function becomes more pronounced, and the errors on the source parameters are actually smaller than the ones obtained by using the simple long wavelength approximation, that is the ratios $(\Delta A/A)_L/(\Delta A/A)$, $(\Delta\Omega_N)_L/\Delta\Omega_N$ and $(\Delta\Omega_L)_L/\Delta\Omega_L$ become all greater than 1. This is clearly due to the structure of the signal recorded at the detector which is amplitude and phase modulated in a characteristic way that depends on the frequency and source position in the sky. In other words the actual LISA output provides more discriminating power than the one inferred from the simple long wavelength approximation. The values of the mean and median of $(\Delta A/A)_L/(\Delta A/A)$, $(\Delta\Omega_N)_L/\Delta\Omega_N$ and $(\Delta\Omega_L)_L/\Delta\Omega_L$ are all greater than 1 (*i.e.* the rigid adiabatic approximation provides errors smaller than the long wavelength approximation) and increase as the emission frequency increases (the higher the frequency the stronger the modulations, cf Figs. 1 and 2). Also the fraction of points for which the above ratios are larger than 1 increases. For $f < 10$ mHz the difference in results between the

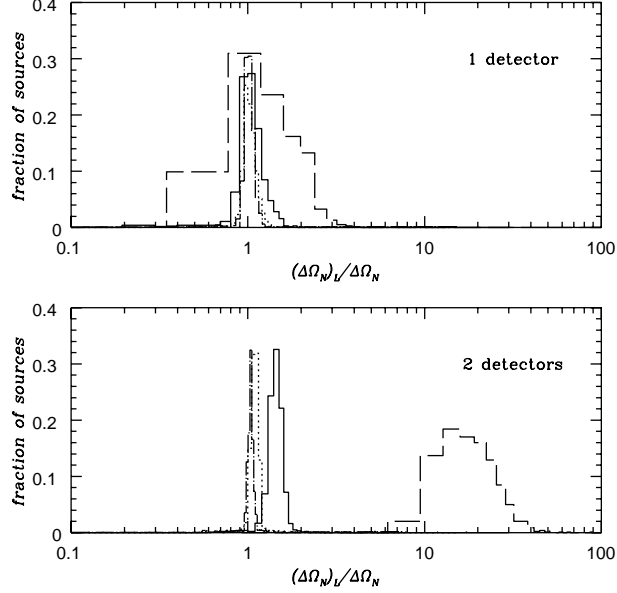


FIG. 6: Distribution of the ratio between the errors associated with measurements of LISA's angular resolution using the long wavelength approximation and the rigid adiabatic approximation. The histograms show the fraction of sources that can be resolved in the sky with an angular resolution characterised by a given value of the ratio $(\Delta\Omega_N)_L/\Delta\Omega_N$, shown on the x -axis (see text for more details). The parameters are the same as the ones in Figure 5. A statistical summary of these results is presented in Table III.

ι	f (mHz)	$(\Delta\Omega_N)_L/\Delta\Omega_N$					
		Min.	Max.	Median	Mean	Std. Dev.	Fraction < 1
I	3	0.353	7.606	1.011	1.035	0.282	0.418
I+II	3	0.560	10.666	1.036	1.062	0.366	0.185
I	5	0.292	7.737	1.019	1.047	0.290	0.403
I+II	5	0.561	11.832	1.099	1.127	0.408	0.380
I	10	0.208	8.144	1.045	1.089	0.331	0.360
I+II	10	0.676	17.225	1.446	1.490	0.602	0.010
I	30	0.345	14.790	1.354	1.487	0.838	0.243
I+II	30	6.808	259.199	18.908	20.586	12.545	0.0

TABLE III: Statistical summary of the values of $(\Delta\Omega_N)_L/\Delta\Omega_N$ obtained in each of the Monte Carlo simulations. The parameters of the simulations are the same as the ones described in Table II. We refer the reader to the former table for more details. Histograms for the distribution of $(\Delta\Omega_N)_L/\Delta\Omega_N$ are presented in Figure 6.

long wavelength approximation and the rigid adiabatic approximation is (on average) $\approx 5 - 15\%$. For $f \geq 10$ mHz the discrepancy in the errors becomes much more pronounced. The difference in errors provided by the two different approximations is particularly strong when one considers the potential of LISA to behave as two interferometers with uncorrelated outputs: at 10 mHz and 30 mHz respectively the errors are actually 50% and a factor ~ 10 smaller than the ones obtained using the long wavelength approximation. However, it is important to stress – cf the spread in the histograms in Figures 5, 6 and 7, and the minimum and maximum value of $(\Delta A/A)_L/(\Delta A/A)$, $(\Delta\Omega_N)_L/\Delta\Omega_N$ and $(\Delta\Omega_L)_L/\Delta\Omega_L$ in Table II, III and IV – that if one considers any given source, even at $f_0 = 3$ mHz or 5 mHz right in the heart of the LISA sensitivity band where one would expect the long wavelength approximation to be completely adequate, the difference in the value of the errors can range from $\approx 30\%$ to a factor ≈ 10 . Moreover, depending on

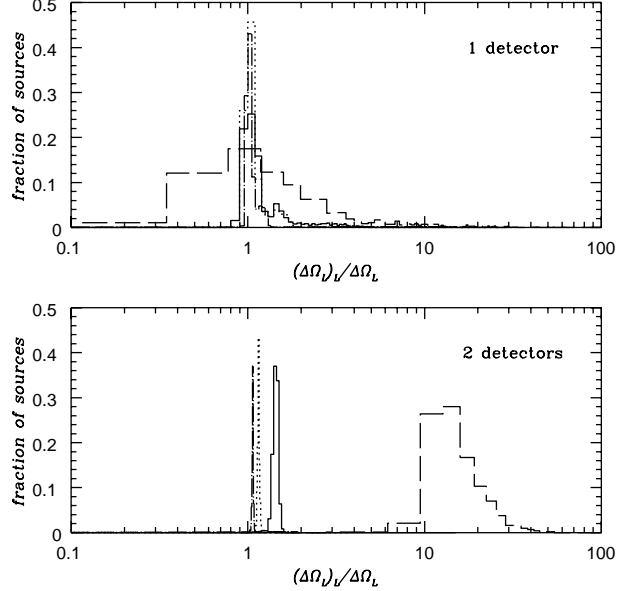


FIG. 7: Distribution of the ratio between the errors associated with the measurements of the orientation of the binary orbital plane using the long wavelength approximation and the rigid adiabatic approximation. The histograms show the fraction of sources whose orbital plane orientation, described by the unit vector $\hat{\mathbf{L}}$ (cf the Appendix) can be resolved within a solid angle characterised by a given value of the ratio $(\Delta\Omega_L)_L/\Delta\Omega_L$, shown on the x -axis (cf text for more details). The parameters are the same as the ones in Figures 5 and 6. A statistical summary of these results is presented in Table IV

ι	f (mHz)	$(\Delta\Omega_L)_L/\Delta\Omega_L$					
		Min.	Max.	Median	Mean	Std. Dev.	Fraction < 1
I	3	0.422	1.384	1.017	1.043	0.077	0.295
I + II	3	0.995	1.086	1.033	1.032	0.010	0.006
I	5	0.915	2.312	1.036	1.110	0.192	0.260
I + II	5	1.011	1.154	1.094	1.092	0.016	0.0
I	10	0.825	5.187	1.105	1.440	0.777	0.235
I + II	10	1.062	1.614	1.442	1.435	0.053	0.0
I	30	0.247	61.811	1.856	4.746	7.429	0.211
I + II	30	5.988	52.498	15.150	16.941	6.567	0.0

TABLE IV: Statistical summary of the values of $(\Delta\Omega_L)_L/\Delta\Omega_L$ obtained in each of the Monte Carlo simulations. The parameters of the simulations are the same as the ones described in Tables II and III. We refer the reader to the former tables for more details. Histograms for the distribution of $(\Delta\Omega_L)_L/\Delta\Omega_L$ are presented in Figure 7.

the source geometrical parameters, the actual errors (the ones derived using the rigid adiabatic approximation) could be *larger* than the ones predicted using the long wavelength approximation. For detailed studies of LISA astronomy it is therefore important to consider the real response of the instrument even in the mHz range.

We would like to conclude this discussion by pointing out another subtlety. So far we have concentrated on the comparison of the lower bounds on the minimum mean squared errors estimated using two different expressions of the detector output. The conclusion is that the full transfer function needs to be included in order to obtain accurate predictions of the quality of LISA astronomy. If one sticks to the long wavelength approximation as a model of the detector output, such predictions become increasingly less accurate as the frequency of the putative source increases. We have therefore argued that the errors are (on average) actually smaller than the ones reported so far in the

literature. However, the actual errors with which LISA will be able measure source parameters do not necessarily decrease at higher frequencies: in fact, for a given distance, position and orientation in the sky of a monochromatic source, when the frequency increases also the LISA noise spectral density becomes larger (which in turn degrades the quality of measurements). There is therefore a competition of effects, and it is simple to show that eventually the signal-to-noise degradation “wins” over richness of signal structure.

V. CONCLUSIONS

We have explored the effect of the LISA transfer function on signal detection and parameter estimation for monochromatic sources. We have shown that for signal detection, although the long wavelength approximation is not a faithful representation of the Michelson interferometer output for $f \gtrsim 3$ mHz, it can actually be safely used in constructing templates for monochromatic signals up to 10 mHz. The fitting-factor, in fact, always exceeds 0.97 in this frequency regime. For parameter estimation, on the other hand, the effects of the frequency and position dependent transfer function already become significant around 3-to-5 mHz and the use of the long wavelength approximation is totally inappropriate for $f \gtrsim 10$ mHz: the estimate of the measurement errors can be quite different, ranging from 5% to a factor ~ 10 (or more), from the ones obtained using the low frequency approximation depending on the source parameters and the observational mode (LISA as a 2 or 3 arm instrument). Our analysis is limited in two main respects. In the study of signal detection we have explored the parameter space quite extensively for the calculation of the match, but not for the fitting factor; this is entirely due to the computational constraints, but can be alleviated in the future by accommodating longer runs. Secondly, both for parameter estimation and signal detection, we have restricted attention only to monochromatic signals. If the source chirp mass is, say, $1 M_\odot$ and the observation time 1 yr, the radiation becomes linearly chirping at $f \approx 5$ mHz. This introduces an additional parameter (the first time derivative of the frequency) in the signal gravitational wave phase. The transition to a linearly chirping regime depends on the source chirp mass and is at higher frequencies for white dwarf binary systems. Therefore, depending on the source mass that is considered, the analysis presented in this paper might require the addition of one parameter in the signal waveform. However, it is clear that the results presented here would not be affected in any significant way, and the general conclusions regarding the effect of the transfer function would apply. We plan to return to these issues in a future paper.

Acknowledgments

We would like to thank C. Cutler for several discussions about LISA observations. We are also grateful to A. Mercer, C. Messenger and R. Vallance for assisting us in the early stages of implementation of the Monte Carlo simulations on Tsunami.

APPENDIX A: FORMULAE

Here we present explicit analytical expressions for the rigid adiabatic approximation $h(t)$, see Eqs. (15)-(18), and the long wavelength approximation $h_L(t)$, see Eqs. (21)-(24), to the LISA detector output that are discussed in Section II.

It is convenient to introduce two Cartesian reference frames (cf, *e.g.*, [7]): a “barycentric” frame (x, y, z) tied to the Ecliptic and centred in the Solar System Barycentre, with $\hat{\mathbf{z}}$ perpendicular to the Ecliptic, and the plane (x, y) in the Ecliptic itself; a detector reference frame (x', y', z') , centred in the LISA centre of mass and attached to the detector, with $\hat{\mathbf{z}}'$ perpendicular to the plane defined by the three arms and the x' and y' axis defined so that the unit vectors $\hat{\mathbf{l}}_j$ ($j = 1, 2, 3$) along each arm read

$$\begin{aligned} \hat{\mathbf{l}}_j &= \cos \left[\frac{\pi}{12} + \frac{\pi}{3} (j-1) \right] \hat{\mathbf{x}}' + \sin \left[\frac{\pi}{12} + \frac{\pi}{3} (j-1) \right] \hat{\mathbf{y}}' \\ &= \left[\frac{1}{2} \sin \alpha_j(t) \cos \Phi(t) - \cos \alpha_j(t) \sin \Phi(t) \right] \hat{\mathbf{x}} \\ &\quad + \left[\frac{1}{2} \sin \alpha_j(t) \sin \Phi(t) + \cos \alpha_j(t) \cos \Phi(t) \right] \hat{\mathbf{y}} + \left[\frac{\sqrt{3}}{2} \sin \alpha_j(t) \right] \hat{\mathbf{z}}, \end{aligned} \quad (A1)$$

where $\alpha_j(t)$ increases linearly with time, according to

$$\alpha_j(t) = n_\oplus t - (j-1)\pi/3 + \alpha_0. \quad (A2)$$

In the previous expression α_0 is a constant specifying the orientation of the arms at the arbitrary reference time $t = 0$, and $n_{\oplus} \equiv 2\pi/1 \text{ yr}$. In the Ecliptic frame the motion of LISA's centre-of-mass is described by the polar angles

$$\begin{aligned}\Theta &= \frac{\pi}{2}, \\ \Phi(t) &= \Phi_0 + n_{\oplus}t,\end{aligned}\quad (\text{A3})$$

and the normal to the detector plane $\hat{\mathbf{z}}'$ precesses around $\hat{\mathbf{z}}$ according to

$$\hat{\mathbf{z}}' = \frac{1}{2}\hat{\mathbf{z}} - \frac{\sqrt{3}}{2}[\cos\Phi(t)\hat{\mathbf{x}} + \sin\Phi(t)\hat{\mathbf{y}}]. \quad (\text{A4})$$

We shall follow the convention that primed and unprimed quantities refer to the frame attached to LISA and the Solar System Barycentre, respectively. The geometry of a binary system with respect to LISA is described by the two unit vectors $\hat{\mathbf{N}}$ and $\hat{\mathbf{L}}$, where the former identifies the source position in the sky and the latter defines the direction of the orbital angular momentum (spins are negligible for sub-solar mass binary systems and $\hat{\mathbf{L}}$ can be therefore regarded as constant). With respect to an observer on LISA, i.e. the reference frame (x', y', z') , the polar coordinates of $\hat{\mathbf{N}}$ and $\hat{\mathbf{L}}$ are (θ'_N, ϕ'_N) and (θ'_L, ϕ'_L) , respectively. We also define ψ' as the time dependent polarisation angle. The angles θ'_N , ϕ'_N and ψ' can be written as a function of the angles measured with respect to the solar system barycentre as

$$\cos\theta'_N(t) = \frac{1}{2}\cos\theta_N - \frac{\sqrt{3}}{2}\sin\theta_N\cos(\Phi(t) - \phi_N), \quad (\text{A5})$$

$$\phi'_N(t) = \Xi_1 + \frac{\pi}{12} + \tan^{-1}\left\{\frac{\sqrt{3}\cos\theta_N + \sin\theta_N\sin(\Phi(t) - \phi_N)}{2\sin\theta_N\sin(\Phi(t) - \phi_N)}\right\}, \quad (\text{A6})$$

$$\tan\psi'_N = \frac{\hat{\mathbf{L}} \cdot \hat{\mathbf{z}}' - (\hat{\mathbf{L}} \cdot \hat{\mathbf{N}})(\hat{\mathbf{z}}' \cdot \hat{\mathbf{N}})}{\hat{\mathbf{N}} \cdot (\hat{\mathbf{L}} \times \hat{\mathbf{z}}')}, \quad (\text{A7})$$

where

$$\Xi_j = n_{\oplus}t - \frac{\pi}{12} - \frac{\pi}{3}(j-1) + \Xi_0, \quad (\text{A8})$$

and Ξ_0 sets the orientation of $\hat{\mathbf{l}}_j$ at $t = 0$.

The relevant scalar and vector products entering the definition of ψ' are

$$\hat{\mathbf{L}} \cdot \hat{\mathbf{z}}' = \frac{1}{2}\cos\theta_L - \frac{\sqrt{3}}{2}\sin\theta_L\cos(\Phi(t) - \phi_L), \quad (\text{A9})$$

$$\hat{\mathbf{L}} \cdot \hat{\mathbf{N}} = \cos\theta_L\cos\theta_N + \sin\theta_L\sin\theta_N\cos(\phi_L - \phi_N), \quad (\text{A10})$$

$$\begin{aligned}\hat{\mathbf{N}} \cdot (\hat{\mathbf{L}} \times \hat{\mathbf{z}}') &= \frac{1}{2}\sin\theta_N\sin\theta_L\sin(\phi_L - \phi_N) \\ &\quad - \frac{\sqrt{3}}{2}\cos\Phi(t)(\cos\theta_L\sin\theta_N\sin\phi_N - \cos\theta_N\sin\theta_L\sin\phi_L) \\ &\quad - \frac{\sqrt{3}}{2}\sin\Phi(t)(\cos\theta_N\sin\theta_L\cos\phi_L - \cos\theta_L\sin\theta_N\cos\phi_N).\end{aligned}\quad (\text{A11})$$

The scalar products $\hat{\mathbf{l}}_j \cdot \hat{\mathbf{N}}$ ($j = 1, 2, 3$) entering the expression of the LISA transfer function, Eqs (8), (10a)-(10d) and (11a)-(11d) can be computed in a straightforward way using Eqs. (A1), (A6) and (A7).

The wave polarisation amplitudes, that enter the expressions (16), (18), (22) and (24), are given by

$$A_+(t) = 2\frac{\mathcal{M}^{5/3}}{D}\left[1 + (\hat{\mathbf{L}} \cdot \hat{\mathbf{N}})^2\right](\pi f)^{2/3}, \quad (\text{A12a})$$

$$A_{\times}(t) = -4\frac{\mathcal{M}^{5/3}}{D}(\hat{\mathbf{L}} \cdot \hat{\mathbf{N}})(\pi f)^{2/3}, \quad (\text{A12b})$$

where \mathcal{M} is the source chirp mass, defined as $\mathcal{M} = m^{2/5}\mu^{3/5} - m$ and μ are the total and reduced mass of a binary systems, respectively $-$, f is the GW frequency and D is the (luminosity) distance. The GW phase in Eqs. (17) and (23) is $\phi_{\text{GW}}(t) = 2\pi f_0 t - \phi_0$.

The Doppler phase modulation, in Eqs. (14), (17) and (23), is

$$\varphi_D(t) = 2\pi R_\oplus f \sin \theta_N \cos(\Phi(t) - \phi_N), \quad (\text{A13})$$

where $R_\oplus = 1 \text{ AU}$.

[1] P. L. Bender et al., *LISA Pre-Phase A Report; Second Edition*, MPQ 233 (1998). P. L. Bender et al., *LISA – System and Technology Study Report*, ESA-SCI(2000)11, (2000). <http://www.lisa.jpl.gov>

[2] C. Cutler and K. S. Thorne, *An Overview of Gravitational-Wave Sources*, to appear in Proceedings of GR16 (Durban, South Africa, 2001), gr-qc/0204090.

[3] D. Hils, P. L. Bender, and R. F. Webbink, *ApJ* **360**, 75 (1990).

[4] G. Nelemans, L. R. Yungelson and S. F. Portegies Zwart, *MNRAS* **349**, 181 (2004)

[5] P. L. Bender and D. Hils, *Class. Quantum Grav.* **14**, 1439 (1997).

[6] G. Nelemans, L. R. Yungelson, and S. F. Portegies Zwart, *AA* **375**, 890 (2001)

[7] C. Cutler, *Phys. Rev. D* **57**, 7089 (1998).

[8] R. Takahashi and N. Seto, *ApJ* **575**, 1030 (2002)

[9] N. Seto, *MNRAS* **333**, 469 (2002)

[10] A. Cooray, A. J. Farmer and N. Seto, *ApJ* **601**, L47 (2004)

[11] A. Cooray and N. Seto, *Phys. Rev. D* **69**, 103502 (2004)

[12] N. J. Cornish and L. J. Rubbo, *Phys. Rev. D* **67**, 022001 (2003).

[13] L. J. Rubbo, N. J. Cornish and O. Poujade gr-qc/0311069 (to appear in *Phys. Rev. D*)

[14] C. Cutler and A. Vecchio *Laser Interferometer Space Antenna*, ed. W. M. Falkner (AIP Conference Proceedings 456), pp. 95-100 (1998).

[15] N. Seto, *Phys. Rev. D* **66**, 122001 (2002).

[16] M. Tinto, J. W. Armstrong and F. B. Estabrook, *Phys. Rev. D* **63**, 021101 (2001).

[17] K.S. Thorne, in *300 Years of Gravitation*, edited by S. W. Hawking and W. Israel (Cambridge University Press, Cambridge, England, 1987), pp. 330-458.

[18] L. A. Wainstein and V. D. Zubakov, *Extraction of signals from noise*, Dover, New York (1962).

[19] C.W. Helstrom, *Statistical Theory of Signal Detection*, 2nd edition, Pergamon Press, London (1968).

[20] T.A. Apostolatos, *Phys. Rev. D* **54**, 2421 (1996).

[21] P. Jaranowski, A. Królak, and B. F. Schutz, *Phys. Rev. D* **58**, 063001 (1998).

[22] A. Królak, M. Tinto and M. Vallisneri, submitted to *Phys. Rev. D* (gr-qc/0401108)

[23] The Monte Carlo simulations presented in this paper have been carried out on the Tsunami Beowulf cluster at the University of Birmingham. Tsunami consists of 212 CPUs. Each run took between a few hours and a few days to complete, depending on the parameters of the simulation. For more details on Tsunami see <http://www.sr.bham.ac.uk/tsunami>

[24] L. S. Finn, *Phys. Rev. D* **46**, 5236 (1992).

[25] D. Nicholson and A. Vecchio, *Phys. Rev. D* **57**, 4588 (1998).